MNRAS **430,** 3422–3431 (2013) doi:10.1093/mnras/stt140

Thermal emission at 3.6–8 μm from WASP-19b: a hot Jupiter without a stratosphere orbiting an active star

D. R. Anderson,[1]★ A. M. S. Smith,[1] N. Madhusudhan,[2] P. J. Wheatley,[3] A. Collier Cameron,[4] C. Hellier,[1] C. Campo,[5] M. Gillon,[6] J. Harrington,[5] P. F. L. Maxted,[1] D. Pollacco,[7] D. Queloz,[8] B. Smalley,[1] A. H. M. J. Triaud[8] and R. G. West[9]

[1]*Astrophysics Group, Keele University, Staffordshire ST5 5BG, UK*
[2]*Department of Astrophysical Sciences, Princeton University, Princeton, NJ 08544, USA*
[3]*Department of Physics, University of Warwick, Coventry CV4 7AL, UK*
[4]*School of Physics and Astronomy, University of St. Andrews, North Haugh, Fife KY16 9SS, UK*
[5]*Planetary Sciences Group, Department of Physics, University of Central Florida, Orlando, FL 32816-2385, USA*
[6]*Institut d'Astrophysique et de Géophysique, Université de Liège, Allée du 6 Août, 17, Bat. B5C, Liège 1, Belgium*
[7]*Astrophysics Research Centre, School of Mathematics and Physics, Queen's University, University Road, Belfast BT7 1NN, UK*
[8]*Observatoire de Genève, Université de Genève, 51 Chemin des Maillettes, 1290 Sauverny, Switzerland*
[9]*Department of Physics and Astronomy, University of Leicester, Leicester LE1 7RH, UK*

Accepted 2013 January 22. Received 2013 January 21; in original form 2011 December 21

ABSTRACT

We report detection of thermal emission from the exoplanet WASP-19b at 3.6, 4.5, 5.8 and 8.0 μm. We used the InfraRed Array Camera on the *Spitzer Space Telescope* to observe two occultations of WASP-19b by its host star. We combine our new detections with previous measurements of WASP-19b's emission at 1.6 and 2.09 μm to construct a spectral energy distribution of the planet's dayside atmosphere. By comparing this with model-atmosphere spectra, we find that the dayside atmosphere of WASP-19b lacks a strong temperature inversion. As WASP-19 is an active star ($\log R'_{\rm HK} = -4.50 \pm 0.03$), this finding supports the hypothesis of Knutson, Howard and Isaacson that inversions are suppressed in hot Jupiters orbiting active stars. The available data are unable to differentiate between a carbon-rich and an oxygen-rich atmosphere.

Key words: methods: data analysis – techniques: photometric – occultations – planets and satellites: atmospheres – planets and satellites: individual: WASP-19b – stars: individual: WASP-19.

1 INTRODUCTION

By observing the occultation of an exoplanet by its host star, we can measure the emergent flux from the planet's dayside atmosphere. Such measurements are challenging due to the low planet-to-star flux ratio (for the best cases, typically a few tenths of one per cent in the near-infrared) and sources of noise both instrumental and stellar in origin (e.g. Knutson et al. 2008; Smith et al. 2011). To date, most such measurements (including the first, Charbonneau et al. 2005; Deming et al. 2005) have been made with the *Spitzer Space Telescope*, though ground-based facilities are now an essential complement (e.g. de Mooij & Snellen 2009; Sing & López-Morales 2009).

With a single occultation we can measure the corresponding brightness temperature and determine the eccentricity of the planet's orbit (e.g. Charbonneau et al. 2005), which is necessary for the accurate determination of the stellar and planetary radii in transiting systems (Anderson et al. 2012) and is important for studies of the formation and tidal inflation of short-period, giant planets (e.g. Ibgui, Burrows & Spiegel 2010; Nagasawa & Ida 2011).

With photometric measurements at various wavelengths, we can construct a spectral energy distribution (SED) of the planet's dayside atmosphere. From this we can infer properties such as the planetary albedo, the dayside energy budget and the efficiency of dayside-to-nightside energy redistribution (e.g. Barman, Hauschildt & Allard 2005). As the atmospheric depth probed depends on the molecular opacity in the observation band, a spectrum can describe an atmosphere's vertical temperature structure. The observation that some planet atmospheres exhibit strong temperature inversions, or

★E-mail: dra@astro.keele.ac.uk

stratospheres, and others do not (see Knutson, Howard & Isaacson 2010 for a summary) led to a suggestion that inversions are present in atmospheres hot enough to maintain high-opacity absorbers in the gas phase in the upper atmosphere (e.g. Fortney et al. 2008). However, this was challenged by recent contrary results (Machalek et al. 2008; Fressin et al. 2010) and theory (e.g. Spiegel, Silverio & Burrows 2009). As an alternative, Knutson et al. (2010) suggested that those planets orbiting chromospherically active stars lack inversions because the associated high UV flux destroys the high-opacity, high-altitude compounds that would otherwise induce inversions. This hypothesis is based on a small sample and further measurements across a wider parameter space are vital to test it. Specifically, there is a paucity of measurements for planets orbiting active stars. We suggest composition could be a key factor, with low-metallicity planets lacking high concentrations of the high-opacity absorbers, such as TiO and sulphur, thought to be responsible for inversions (e.g. Fortney et al. 2008; Zahnle et al. 2009).

As the spectral coverage increases, so too does the information about an atmosphere that we can discern. Madhusudhan et al. (2011a) used seven measurements of the emission of WASP-12b (Campo et al. 2011; Croll et al. 2011) to show that the dayside atmosphere is the first known to be carbon dominated. Thus, we are entering an era in which we can make statistically sound inferences about the composition of exoplanet atmospheres. Further, Madhusudhan et al. (2011a) demonstrated that the planet lacks a prominent thermal inversion and has very inefficient day–night energy circulation.

In this paper, we present *Spitzer* measurements of WASP-19b's dayside thermal emission at 3.6, 4.5, 5.8 and 8.0 μm. Discovered by the Wide Angle Search for Planets (WASP; Pollacco et al. 2006; Hebb et al. 2010), the shortest period hot Jupiter, WASP-19b, is a 1.17-$M_{\rm Jup}$ planet in a near-circular, 19-h orbit around a G8V star. Hellier et al. (2011) showed the planet's orbital axis to be aligned with the spin axis of its host star. The planet's thermal emission was previously measured at 1.6 and 2.09 μm (Anderson et al. 2010; Gibson et al. 2010), thus we bring the measurement tally to six bands. We use all six thermal emission measurements to characterize the planet's atmosphere and refine the system parameters by combining these data with pre-existing photometry of the transit and radial-velocity (RV) data.

2 NEW OBSERVATIONS

We observed two occultations of the planet WASP-19b by its host star WASP-19 (2MASS 15595095−2803422, $K_s = 10.22$) with *Spitzer* (Werner et al. 2004) during UT 2009 January 29 and March 22. On each date, we employed the Infrared Array Camera (IRAC; Fazio et al. 2004) in a full array mode (256 × 256 pixels, 1.2 arcsec pix^{-1}). During the first occultation, we measured the WASP-19 system simultaneously in the 4.5- and 8.0-μm channels (respectively, channels 2 and 4) for a duration of 3.2 h. We measured the second occultation simultaneously in the 3.6- and 5.8-μm channels (respectively, channels 1 and 3) for a duration of 3.0 h.

Prior to the first occultation, we used the emission nebula NGC 7538 in Cepheus to 'pre-flash' the target position on the detector arrays for 0.5 h. This was intended to reduce or remove the known illumination-history dependence of the gain response of the 8.0-μm detector (e.g. Knutson et al. 2008 and references therein). The 5.8-μm detector is known to suffer a similar issue, but pre-flashing this array was not permitted due to the detrimental effect it is known to have on the array. Instead, we attempted to stabilize the array by observing the target for an extra hour prior to the occultation. As this 'pre-stare' was performed as a separate observation request to the occultation observation, the target was reacquired between the two. As such, the pre-stare observation must be treated as a separate data set with its own systematics and so are of little use in determining the occultation depth.

Using an effective integration time of 10.4 s, we obtained 876 and 840 images, respectively, for the first and second occultations. In each data set, we see a small, periodic pointing wobble ($P \approx 1$ h), thought to be caused by the thermal cycling of an onboard battery heater.[1] There is also a very small drift of the target position over the span of each data set.

We used the images calibrated by the standard *Spitzer* pipeline (version S18.7.0) and delivered to the community as Basic Calibrated Data. Our method is essentially the same as we presented in Anderson et al. (2011b), to which we refer the reader for further information. For each image, we converted flux from MJy sr^{-1} to electrons and then used IRAF to perform aperture photometry for WASP-19, using circular apertures with a range of radii: 1.5–6 pixels for the 3.6- and 4.5-μm data, and 1–5 pixels for the 5.8- and 8.0-μm data. The apertures were centred by fitting a Gaussian profile on the target. The sky background was measured in an annulus extending from 8 to 12 pixels from the aperture centre, and was subtracted from the flux measured within the on-source apertures. We estimated the photometric uncertainty as the quadrature addition of the uncertainty in the sky background (estimated as the standard deviation of the flux in the sky annulus) in the on-source aperture, the read-out noise and the Poisson noise of the total background-subtracted counts within the on-source aperture. We calculated the mid-exposure times in the HJD (UTC) time system from the MHJD_OBS header values, which are the start times of the Data Collective Events (DCEs), by adding half of a DCE duration (FRAMTIME).

The choice of aperture radius for each data set was a compromise between maximizing the signal-to-noise (S/N) ratio of the measurements and, from fits to all available data (see Section 3), minimizing the residual scatter of the light curve. Each consideration suggested very similar optimal aperture radii and we adopted 2.7 pix for the 3.6- and 4.5-μm data, and 2.5 pix for the 5.8- and 8.0-μm data. For each data set, we found that the variation in the fitted occultation depth (see Section 3) was much smaller than 1σ over a wide range of aperture radii.

Some groups choose to reject a portion of data at the beginning of each observation, citing as justification either the settling of the spacecraft (not seen in our data) or an improvement in the fit; we found no reason to do this. We rejected any flux measurement that was discrepant with the median of its 20 neighbours (a window width of 4.4 min) by more than four times its theoretical error bar. We also performed a rejection on target position. For each image and for the x and y detector coordinates separately, we computed the difference between the fitted target position and the median of its 20 neighbours. For each data set, we then calculated the standard deviation, σ, of these *median differences* and rejected any points discrepant by more than 4σ. The numbers of points rejected on flux and target position for each data set are displayed in Table 1. According to the IRAC handbook, each IRAC array receives approximately 1.5 solar-proton and cosmic ray hits per second, with ∼2 pixels per hit affected in channels 1 and 2, and ∼6 pixels per hit affected in channels 3 and 4, and the cosmic ray flux varies randomly by up to a factor of a few over time-scales

[1] http://ssc.spitzer.caltech.edu/warmmission/news/21oct2010memo.pdf

Table 1. Number of points rejected per data set per criterion.

Data set	Flux	*x*-pos	*y*-pos	Total (per cent)
2009 Mar 22 / 3.6 μm	8	1	3	11 (1.3)
2009 Jan 29 / 4.5 μm	11	41	11	51 (5.8)
2009 Mar 22 / 5.8 μm	11	9	7	21 (2.5)
2009 Jan 29 / 8.0 μm	4	8	9	17 (1.9)

of minutes. Thus, the average probability per exposure that pixels within the stellar aperture will be affected by a cosmic ray hit is 1.3 per cent for channels 1 and 2 and 3.2 per cent for channels 3 and 4, which is in good agreement with the portion of frames that we rejected. These probabilities are likely to be underestimates as we calculated them using partial pixels and neglecting the effect of hits within the sky annuli. For an unknown reason, a greater portion of channel 2 images was rejected due to jumps of the target position, particularly in the *x* direction. The post-rejection data are displayed raw and binned in the first and second panels, respectively, of Fig. 1.

3 DATA ANALYSIS

3.1 Data and model

We performed a global determination of the system parameters incorporating: our new *Spitzer* occultation photometry; the HAWK-I *H*-band and 2.09-μm occultation light curves obtained, respectively, by Anderson et al. (2010) and Gibson et al. (2010); the 34 CORALIE RV measurements listed in Hebb et al. (2010); the 36 HARPS RVs, obtained through a transit, and the 3 CORALIE RVs given in Hellier et al. (2011); the LCOGT FTS *z*-band transit light curve from Hebb et al. (2010) and the ESO NTT *r*-band transit light curve presented in Hellier et al. (2011). We did not include the three seasons of WASP survey photometry presented in Hebb et al. (2010). Rather, we placed a Bayesian Gaussian prior on the epoch of mid-transit, T_c, using the epoch given in Hellier et al. (2011): $T_c = 2455\,168.968\,01 \pm 0.000\,09$ HJD. Thus, our analyses completed quicker and the shape of the transit was determined using only the high S/N photometry. This can be preferable as photometry from surveys such as WASP is prone to dilution and, depending on which detrending algorithm is used, the transit depth can be suppressed. We decorrelated each transit light curve with a linear function of time. The HAWK-I *H*-band data were partitioned and detrended as in Anderson et al. (2010) and the HAWK-I 2.09-μm light curve was decorrlelated with a linear function of time as in Gibson et al. (2010). These data were used as input into an adaptive Markov Chain Monte Carlo (MCMC) algorithm (Collier Cameron et al. 2007; Pollacco et al. 2008; Enoch et al. 2010); see Anderson et al. (2011a) for a description of the current version of our code. Such an analysis, incorporating all available data, is necessary to take account of the cross-dependence of system parameters and to make a reliable assessment of their uncertainties. We partitioned the RV

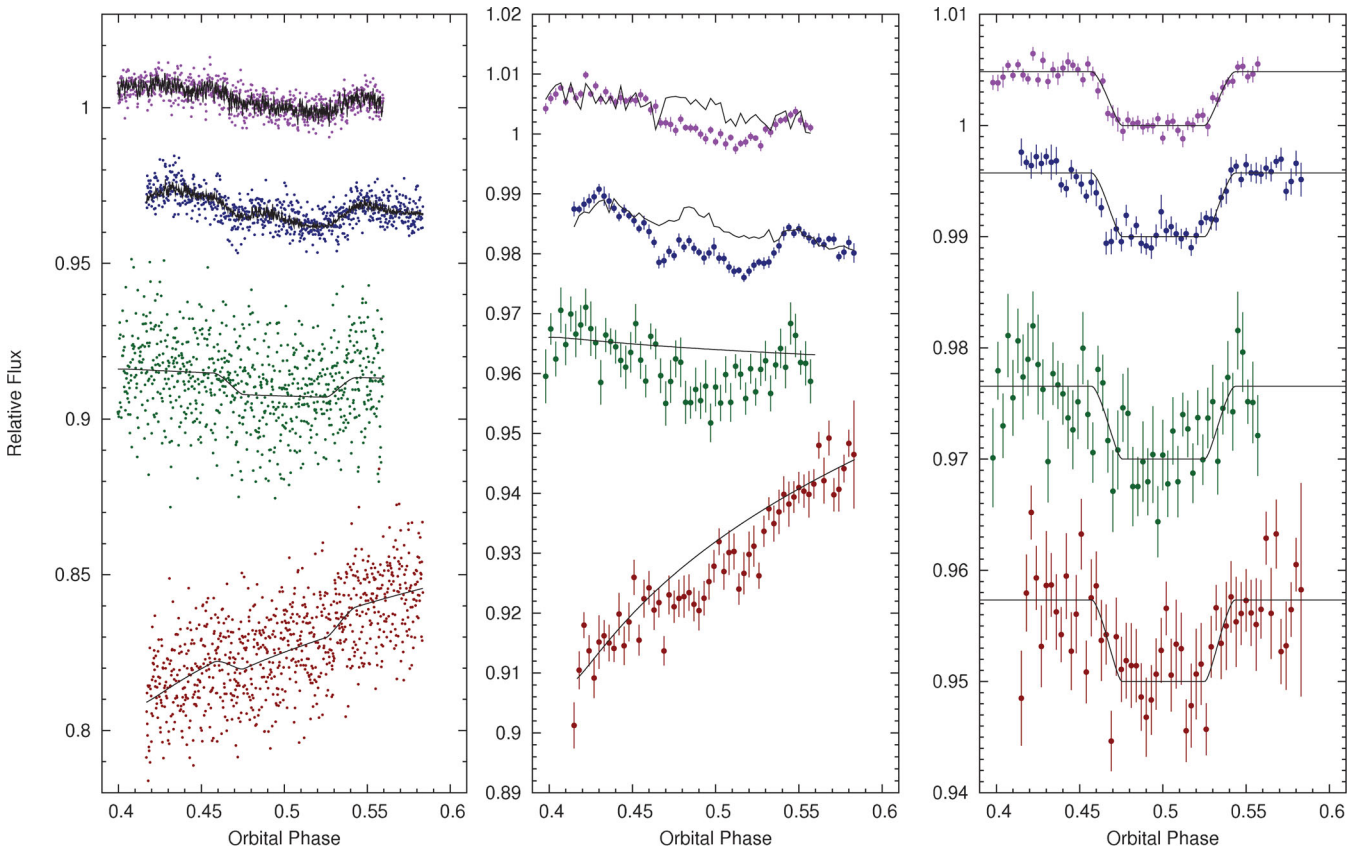

Figure 1. In each of the above three plots, from top to bottom, the data were taken at 3.6, 4.5, 5.8 and 8.0 μm. Relative flux offsets were applied to data sets for clarity. Left: raw *Spitzer* data with the best-fitting trend and occultation models superimposed. Middle: the same data binned in phase ($\Delta\phi = 0.003 \sim 3.4$ min) with the best-fitting trend models superimposed. Right: the binned data after dividing by the best-fitting trend models, and with the best-fitting occultation models superimposed. The error bar on each binned measurement in the panels in the middle and on the right is the standard deviation of the points within the bin.

data by spectrograph so as to allow for an instrumental offset and for a potential specific stellar activity level during the short-baseline HARPS observations.

The MCMC proposal parameters we used are T_c, P, $(R_{pl}/R_*)^2$, T_{14}, b, K_1, T_{eff}, [Fe/H], $\sqrt{e}\cos\omega$, $\sqrt{e}\sin\omega$, $\sqrt{v}\sin i\cos\lambda$, $\sqrt{v}\sin i\sin\lambda$, $\Delta F_{1.6}$, $\Delta F_{2.09}$, $\Delta F_{3.6}$, $\Delta F_{4.5}$, $\Delta F_{5.8}$, $\Delta F_{8.0}$ and t_{off}. See Section 3.2 for a definition of t_{off} and Table 3 for definitions of the other parameters. At each step in the MCMC procedure, each proposal parameter is perturbed from its previous value by a small, random amount. From the proposal parameters, model light and RV curves are generated and χ^2 is calculated from their comparison with the data. A step is accepted if χ^2 (our merit function) is lower than for the previous step, and a step with higher χ^2 is accepted with probability $\exp(-\Delta\chi^2/2)$. In this way, the parameter space around the optimum solution is thoroughly explored. The value and uncertainty for each parameter are, respectively, taken as the median and central 68.3 per cent confidence interval of the parameter's marginalized posterior probability distribution (e.g. Ford 2006).

3.2 *Spitzer* data

IRAC uses an InSb detector to observe at 3.6 and 4.5 μm, and the measured flux exhibits a strong correlation with the position of the target star on the array. This effect is due to the inhomogeneous intrapixel sensitivity of the detector and is well documented (e.g. Knutson et al. 2008 and references therein). Following Charbonneau et al. (2008), we modelled this effect as a quadratic function of the sub-pixel position of the point spread function (PSF) centre, with the addition of a cross-term to permit rotation (Désert et al. 2009) and a linear term in time:

$$\mathrm{d}f = a_0 + a_x\mathrm{d}x + a_y\mathrm{d}y + a_{xy}\mathrm{d}x\mathrm{d}y + a_{xx}\mathrm{d}x^2 + a_{yy}\mathrm{d}y^2 + a_t\mathrm{d}t, \quad (1)$$

where $\mathrm{d}f = f - \hat{f}$ is the stellar flux relative to its weighted mean, $\mathrm{d}x = x - \hat{x}$ and $\mathrm{d}y = y - \hat{y}$ are the coordinates of the PSF centre relative to their weighted means, $\mathrm{d}t$ is the time elapsed since the first observation, and a_0, a_x, a_y, a_{xy}, a_{xx}, a_{yy} and a_t are coefficients.

IRAC uses a SiAs detector to observe at 5.8 and 8.0 μm, and its response is thought to be homogeneous, though another systematic affects the photometry. This effect is known as the 'ramp' because it causes the gain to increase asymptotically over time for every pixel, with an amplitude depending on a pixel's illumination history (e.g. Knutson et al. 2008 and references therein). Again following Charbonneau et al. (2008), we modelled this ramp as a quadratic function of $\ln(\mathrm{d}t)$:

$$\mathrm{d}f = a_0 + a_1\ln(\mathrm{d}t + t_{off}) + a_2(\ln(\mathrm{d}t + t_{off}))^2, \quad (2)$$

where t_{off} is a proposal parameter restricted to positive values. To prevent t_{off} from drifting to values greater than an hour or so, we place on it a Gaussian prior by adding a Bayesian penalty to our merit function (χ^2):

$$BP_{t_{off}} = t_{off}^2/\sigma_{t_{off}}^2, \quad (3)$$

where $\sigma_{t_{off}} = 15$ min.

A steep ramp is evident in the 8.0-μm light curve (Fig. 1, middle panel). Due to the large distance on the sky between the target and the pre-flash source, there was an 11-min gap between the end of the pre-flash observations and the start of the target observations. It may be that the detector traps de-populated during this time, giving rise to the observed ramp that is more typical of observations without pre-flash.

Table 2. Trend model parameters and coefficients.

	3.6 μm	4.5 μm	5.8 μm	8.0 μm
$\hat{f}$	151 194.55	80 580.23	12 693.57	18 991.68
$\hat{x}$	31.93	24.50	25.99	25.44
$\hat{y}$	24.91	25.98	25.16	23.63
a_0	-24 ± 16	89.7 ± 5.0	-95.2^{+26}_{-22}	1569^{+142}_{-116}
a_x	6566 ± 75	-433 ± 36	–	–
a_y	9278 ± 49	4062 ± 32	–	–
a_{xy}	6040 ± 3280	-7860 ± 4150	–	–
a_{xx}	-6330 ± 1230	$23\,000 \pm 880$	–	–
a_{yy}	$-22\,500 \pm 1980$	$30\,360 \pm 3810$	–	–
a_t	1050 ± 270	-2203 ± 57	–	–
a_1	–	–	-52^{+21}_{-11}	800^{+110}_{-86}
a_2	–	–	$-5.9^{+4.1}_{-1.4}$	78^{+18}_{-13}
t_{off}/min	–	–	$10.6^{+11.4}_{-8.1}$	$15.3^{+10.1}_{-7.4}$

In addition to equation (2), we tried trend functions with a variety of time dependences: no time dependence; a linear-logarithmic time dependence [equivalent to setting $a_2 = 0$ in equation (2)]; a linear time dependence and a quadratic time dependence. Each of these functions results in depths consistent within 1σ with the depths obtained using equation (2). For this reason and because equation (2) has been shown to accurately describe the ramp in higher cadence, longer baseline data sets obtained with the SiAs detectors (e.g. Knutson et al. 2009), we adopt equation (2) as our trend model for channels 3 and 4.

We used singular value decomposition (Press et al. 1992) to determine the trend model coefficients by linear least-squares minimization at each MCMC step, subsequent to division of the data by the eclipse model. The best-fitting trend models are superimposed on the binned photometry in the middle panel of Fig. 1. Table 2 gives the best-fitting values for the trend model parameters and coefficients (equations 1 and 2), together with their 1σ uncertainties.

3.3 Photometric and RV noise

We scaled the formal photometric error bars so as to obtain a reduced χ^2 of unity, applying one scale factor per data set. The aim was to properly weight each data set in the simultaneous MCMC analysis and to obtain realistic uncertainties. The error bars of the FTS and the NTT photometry were multiplied, respectively, by 0.71 and 1.15. The scale factors for the error bars of the occultation photometry from IRAC channels 1, 2, 3 and 4 were, respectively, 1.02, 0.99, 1.16 and 1.04. Importantly, the error bars of the occultation photometry were not scaled when deciding which trend models or aperture radii to use. In Anderson et al. (2010), the HAWK-I H-band occultation data were split into 11 light curves according to offset and telescope repointing. Within a global analysis, each light curve was detrended individually and the error bars of each light curve was rescaled by its own factor. As the number of data points in each light curve is small (8–12 in the 6 light curves obtained prior to repointing and 40–44 in the 5 light curves obtained post-repointing), we here opted to rescale the error bars of all 11 light curves by the same factor, which was 1.14, though we did still detrend each light curve separately. The error bars of the 2.09-μm light curve presented in Gibson et al. (2010) were scaled by 6.15. Gibson et al. (2010) also found their uncertainties required a large scaling factor (6.17). They attributed this to variations in the interpixel sensitivity that likely resulted from their random dithering (radius = 30 arcsec) of the pointing between observations. Though our H-band observations were also

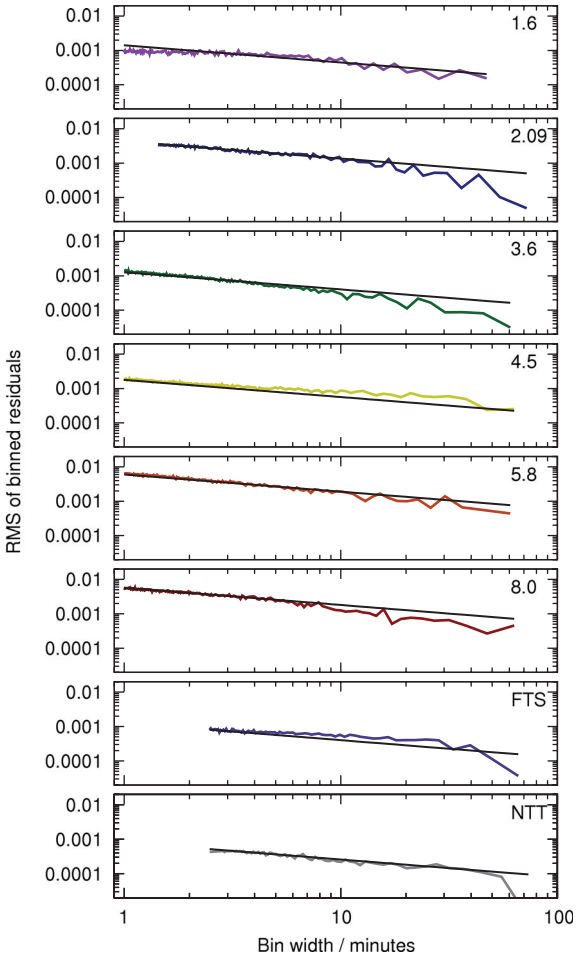

Figure 2. RMS of the binned residuals for, from top to bottom, the pre-existing HAWK-I occultation photometry at 1.6 and 2.1 μm, the new *Spitzer* occultation photometry at 3.6, 4.5, 5.8 and 8.0 μm, and the pre-existing FTS and NTT transit photometry. The solid black lines, which are the rms of the unbinned data scaled by the square root of the number of points in each bin, show the white-noise expectation. The ranges of bin widths are appropriate for the data sets' cadences and durations.

made using HAWK-I (Anderson et al. 2010), the corresponding scale factor was much closer to unity. This is because we dithered over a fixed pattern of six offsets and did not employ random jitter. We could thus produce one light curve per offset position and model each of their systematics independently. Current best practice is to avoid offsetting at all.

We assessed the presence of correlated noise in the occultation and transit data by plotting the rms of their binned residuals (Fig. 2). The 4.5-μm occultation light curve and the FTS transit light curve both display a small amount of correlated noise on time-scales of 5 min and longer.

To obtain a reduced spectroscopic χ^2 of unity and to balance the different data sets in the MCMC, we added in quadrature a jitter of 14.1 m s^{-1} to the uncertainties of the CORALIE RVs and 6.9 m s^{-1} to the uncertainties of the HARPS RVs, as was done in Hellier et al. (2011).

3.4 Time systems and light travel time

The *Spitzer*, HAWK-I, FTS and NTT photometry are in the HJD (UTC) time system. The CORALIE and HARPS RVs are in the BJD (UTC) time system. The difference between BJD and HJD is less than 4 s and so is negligible for our purposes, and the timing information mostly comes from the photometry. Leap second adjustments are made to the UTC system to keep it close to mean solar time, so one should really use Terrestrial Time. However, our observations span a short baseline (2008–2010), during which there was only one leap second adjustment, so our choice to use the UTC system has no impact.

The occultation of WASP-19b occurs farther away from us than its transit does, so we made a first-order correction for the light travel time. We calculated the light travel time between the beginning of occultation ingress and the beginning of transit ingress to be 15 s. We subtracted this from the mid-exposure times of the *Spitzer* and HAWK-I occultation photometry. For comparison, we measure the time of mid-occultation to a 1σ precision of 35 s.

3.5 Results

Table 3 shows the median values and the 1σ uncertainties of the fitted proposal parameters and derived parameters from our final MCMC analysis. Fig. 1 shows the best-fitting trend and occultation models together with the raw and detrended *Spitzer* data. Table 2 gives the best-fitting values for the parameters of the trend models, together with their 1σ uncertainties. Fig. 3 displays all the photometry and RVs used in the MCMC analysis, with the best-fitting eclipse and RV models superimposed.

Anderson et al. (2010) measured an occultation depth of 0.259 ± 0.045 per cent from their *H*-band light curve. In analysing the same data, we obtained a similar depth of 0.276 ± 0.044 per cent. The minor difference is probably due to some combination of the slightly different manner in how the light curves' error bars were rescaled (see Section 3.3) and the slight difference in the occultation ephemeris [the additional RV and occultation data result in a mid-occultation time at the time of the *H*-band observations ∼5 min earlier than found by Anderson et al. (2010)]. The occultation depth of 0.366 ± 0.067 per cent that we derived from the 2.09-μm light curve of Gibson et al. (2010) is near-identical to the depth that they obtained (0.366 ± 0.072 per cent).

We used the residual permutation or 'prayer bead' method (e.g. Gillon et al. 2007) as described in Smith et al. (2012) to assess the impact of any correlated noise present in the occultation light curves on our fitted occultation depths. The occultation depths derived from that analysis are consistent with the depths we measured from the non-permuted light curves and it is the latter that we adopt (Table 4).

We calculated the brightness temperatures that correspond to the measured occultation depths and present these in Table 3. To calculate these, we defined the product of the planet-to-star area ratio and the ratio of the band-integrated planet-to-star flux densities, corrected for the wavelength-dependence of the transmission,[2] to be equal to the measured occultation depth (e.g. Charbonneau et al. 2005). We used a model spectrum of a star with the $T_{\rm eff}$, $\log g$ and [Fe/H] values of Table 3 (Hauschildt, Allard & Baron 1999),

[2] For the HAWK-I measurements, the transmission of the atmosphere, telescope, instrument, and detector were accounted for by using the transmission curve obtained from http://www.eso.org/observing/etc/. For the *Spitzer* measurements, the telescope throughput and detector quantum efficiency were accounted for by using the full array average spectral response curves available at http://irsa.ipac.caltech.edu/data/SPITZER/docs/irac/calibrationfiles/spectralresponse/ .

Table 3. System parameters of WASP-19.

Parameter	Symbol	Value	Unit
Orbital period	P	$0.788\,839\,51 \pm 0.000\,000\,32$	d
Epoch of mid-transit (HJD, UTC)	T_c	$2455\,183.167\,11 \pm 0.000\,068$	d
Transit duration (from first to fourth contact)	T_{14}	$0.065\,49 \pm 0.000\,35$	d
Duration of transit ingress ≈ duration of transit egress	$T_{12} \approx T_{34}$	$0.013\,46 \pm 0.000\,52$	d
Planet-to-star area ratio	$(R_{pl}/R_*)^2$	$0.020\,50 \pm 0.000\,24$	
Impact parameter	b	0.656 ± 0.015	
Orbital inclination	i	79.42 ± 0.39	°
Semi-amplitude of the stellar reflex velocity	K_1	256.9 ± 2.7	m s^{-1}
Centre-of-mass velocity	γ_{rv1}	$20\,787.26 \pm 0.23$	m s^{-1}
Offset between HARPS and CORALIE	$\gamma_{HARPS\text{-}CORALIE}$	19.32 ± 0.82	m s^{-1}
Orbital eccentricity	e	$0.0019^{+0.0055}_{-0.0015}$	
		<0.027 (3σ)	
Argument of periastron	ω	75^{+24}_{-162}	°
	$e\cos\omega$	$0.000\,10^{+0.000\,81}_{-0.000\,69}$	
	$e\sin\omega$	$0.0007^{+0.0062}_{-0.0016}$	
Phase of mid-occultation, having accounted for light travel time	$\phi_{mid\text{-}occ.}$	$0.500\,06^{+0.000\,52}_{-0.000\,44}$	
Occultation duration	T_{58}	$0.065\,64^{+0.000\,43}_{-0.000\,40}$	d
Duration of occultation ingress ≈ duration of occultation egress	$T_{56} \approx T_{78}$	$0.013\,58 \pm 0.000\,54$	d
Relative planet-to-star flux at 1.6 μm	$\Delta F_{1.6}$	0.276 ± 0.044	per cent
Relative planet-to-star flux at 2.09 μm	$\Delta F_{2.09}$	0.366 ± 0.067	per cent
Relative planet-to-star flux at 3.6 μm	$\Delta F_{3.6}$	0.483 ± 0.025	per cent
Relative planet-to-star flux at 4.5 μm	$\Delta F_{4.5}$	0.572 ± 0.030	per cent
Relative planet-to-star flux at 5.8 μm	$\Delta F_{5.8}$	0.65 ± 0.11	per cent
Relative planet-to-star flux at 8.0 μm	$\Delta F_{8.0}$	0.73 ± 0.12	per cent
Planet brightness temperature[a] at 1.6 μm	$T_{b,\,1.6}$	2750 ± 130	K
Planet brightness temperature[a] at 2.09 μm	$T_{b,\,2.09}$	2670 ± 170	K
Planet brightness temperature[a] at 3.6 μm	$T_{b,\,3.6}$	2346 ± 57	K
Planet brightness temperature[a] at 4.5 μm	$T_{b,\,4.5}$	2273 ± 64	K
Planet brightness temperature[a] at 5.8 μm	$T_{b,\,5.8}$	2260 ± 230	K
Planet brightness temperature[a] at 8.0 μm	$T_{b,\,8.0}$	2260 ± 250	K
Sky-projected stellar rotation velocity	$v\sin i$	4.63 ± 0.27	km s^{-1}
Sky-projected angle between stellar spin and planetary orbit axes	λ	4.1 ± 5.2	°
Star mass	M_*	0.969 ± 0.023	$M_\odot$
Star radius	R_*	0.993 ± 0.018	$R_\odot$
Star density	ρ_*	0.990 ± 0.043	$\rho_\odot$
Star surface gravity	$\log g_*$	4.430 ± 0.012	cgs
Star effective temperature	T_{eff}	5475 ± 98	K
Star metallicity	[Fe/H]	0.02 ± 0.09	dex
Planet mass	M_{pl}	1.165 ± 0.023	M_{Jup}
Planet radius	R_{pl}	1.383 ± 0.031	R_{Jup}
Planet density	ρ_{pl}	0.440 ± 0.026	ρ_{Jup}
Planet surface gravity	$\log g_P$	3.133 ± 0.017	cgs
Semimajor axis	a	$0.016\,53 \pm 0.000\,13$	au
Planet equilibrium temperature[b] (full redistribution)	$T_{P,\,A\,=0,\,f\,=1}$	2045 ± 41	K
Planet equilibrium temperature[b] (day side redistribution)	$T_{P,\,A\,=0,\,f\,=2}$	2432 ± 49	K
Planet equilibrium temperature[b] (instant re-radiation)	$T_{P,\,A\,=0,\,f\,=8/3}$	2614 ± 52	K

[a] We modelled both star and planet as black bodies and took account of only the occultation depth uncertainty, which dominates.

[b] $T_{P,\,A\,=0,\,f} = f^{\frac{1}{4}} T_{eff}\sqrt{\frac{R_*}{2a}}$ where f is the redistribution factor, with $f = 1$ for full redistribution, $f = 2$ for dayside redistribution and $f = 8/3$ for instant re-radiation (Cowan & Agol 2011). We assumed the planet albedo to be zero, $A = 0$.

normalized to reproduce the integrated flux of a blackbody with $T_{eff} = 5475$ K. The uncertainties in the brightness temperatures only take into account the uncertainties in the measured occultation depths.

To obtain a reliable determination of the orbital eccentricity, it is important that the time of mid-transit is known with accuracy and precision at the epochs the occultation data are obtained. The WASP photometry, which we used to place a prior on the transit ephemeris, spans a two-year baseline of 2006 May to 2008 May and the FTS transit light curve was obtained in 2008 December. All occultation data were obtained soon after: during 2009 January to April. The NTT transit light curve, obtained in 2010 February, ensures a reliable transit ephemeris at the occultation epochs. We note, though, that the difference between the transit ephemeris presented herein and that presented in the discovery paper (Hebb et al. 2010, i.e. without the NTT light curve), propagated to the occultation epochs, is a mere ∼20 s. The accuracy of the discovery-paper ephemeris is due to the long baseline of the WASP photometry and the high

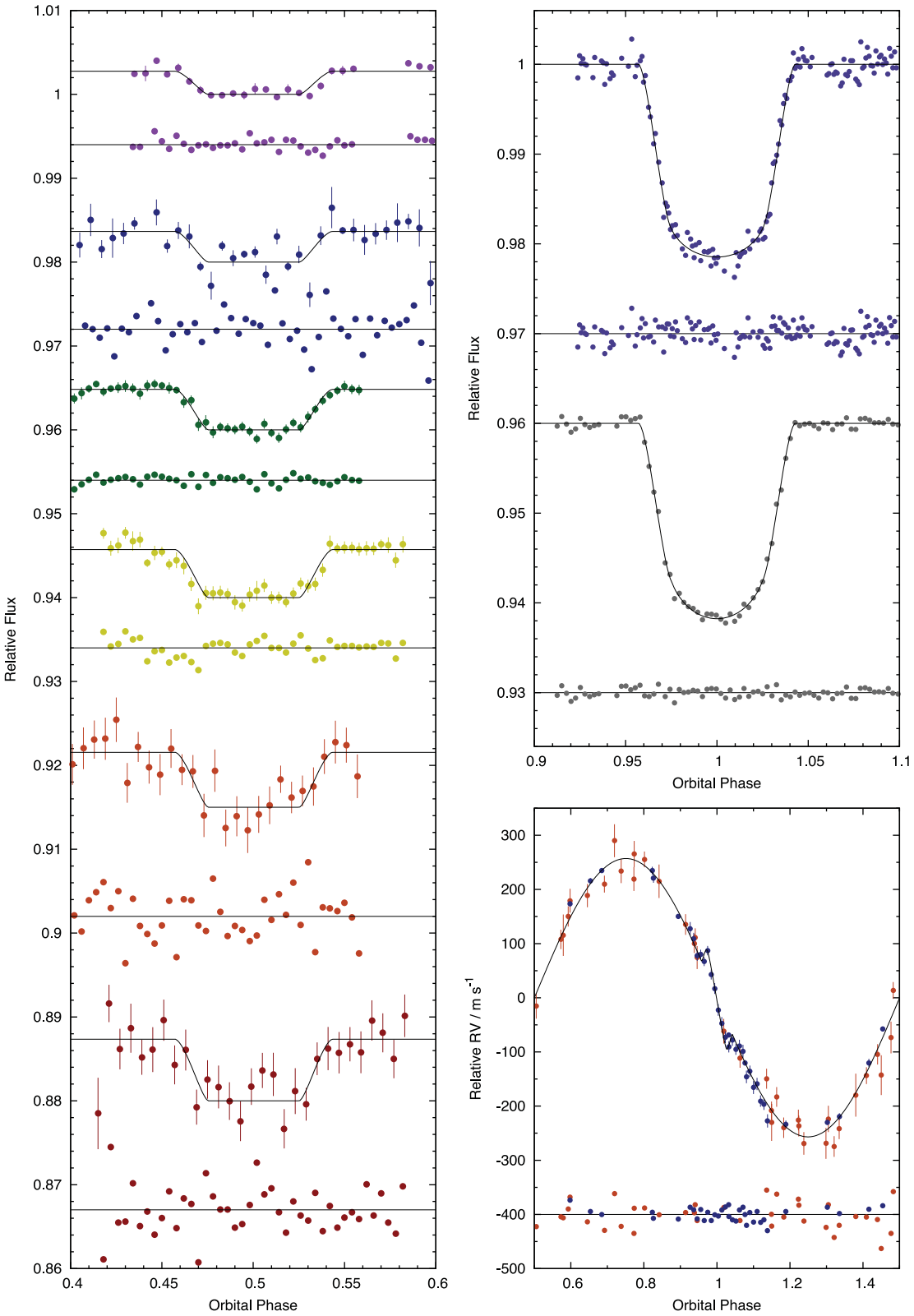

Figure 3. The results of our global analysis, which combines our new *Spitzer* occultation photometry with pre-existing transit photometry, ground-based occultation photometry and radial velocities. The models generated from the best-fitting parameter values of Table 3 are overplotted and the residuals about the models are plotted below each data set. Arbitrary offsets have been applied to the photometry plots for display purposes. Left: from top to bottom, HAWK-I occultations at 1.6 μm (Anderson et al. 2010), 2.09 μm (Gibson et al. 2010) and our IRAC occultations at 3.6, 4.5, 5.8 and 8.0 μm. The error bar on each binned measurement is the standard deviation of the points within the bin. Top right: *z*-band transit light curve taken with FTS (upper; Hebb et al. 2010) and *r*-band transit light curve taken with NTT (lower; Hellier et al. 2011). Bottom right: spectroscopic orbit and transit illustrated by CORALIE and HARPS data (Hebb et al. 2010; Hellier et al. 2011). The measured systemic velocities (Table 3) of each data set have been subtracted.

Table 4. Comparing adopted and permuted occultation depths.

Light curve	Adopted depth	Permuted depth
1.6 μm	0.002 76 ± 0.000 44	0.002 70 + 0.000 95
2.09 μm	0.003 66 ± 0.000 67	0.003 71 + 0.000 35
3.6 μm	0.004 83 ± 0.000 25	0.004 85 + 0.000 18
4.5 μm	0.005 72 ± 0.000 30	0.005 67 + 0.000 71 − 0.000 30
5.8 μm	0.0065 ± 0.0011	0.006 34 ± 0.000 50
8.0 μm	0.0073 ± 0.0012	0.008 24 ± 0.000 77

quality of the FTS light curve, which was obtained only months before the occultation data.

3.6 Stellar activity

Hebb et al. (2010) reported a rotational modulation of the WASP light curves with a period of 10.5 ± 0.2 d and an amplitude of a few mmag. This indicated that WASP-19 is an active star, with the sinusoidal modulation being induced by a non-axisymmetric distribution of starspots.

We determine the log $R'_{\rm HK}$ activity index of WASP-19 by measuring the weak emission in the cores of the Ca II H+K lines (Noyes, Weiss & Vaughan 1984; Santos et al. 2000; Boisse et al. 2009). The 36 HARPS spectra presented in Hellier et al. (2011) had signal-to-noise ratio (SNR) in the range 14–38. We selected the 12 spectra with SNR>19 per pixel at 550 nm, as the activity level tends to be systematically under- or overestimated for spectra with low SNR. By assuming $B - V = 0.570$, we infer $\log R'_{\rm HK} = -4.50 \pm 0.03$, which are the weighted mean and standard deviation of the values determined from individual spectra; we used the SNR as the weighting factor. This is similar to the value of $\log R'_{\rm HK} = -4.66$ measured by Knutson et al. (2010). It is difficult to judge the level at which the two values agree as Knutson et al. (2010) do not provide an uncertainty estimate and our uncertainty value is likely to be an underestimate.

As we know the true stellar rotation period to be 10.5 ± 0.2 d from rotational modulation, we can use our log $R'_{\rm HK}$ value to test the activity–rotation calibration of Mamajek & Hillenbrand (2008). The calibration suggests a stellar-rotation period of $P_{\rm rot} = 12.3 \pm 1.5$ d, which is consistent within errors.

We considered whether stellar variability could have affected our measured occultation depths. One potential issue is that the stellar brightness may have varied significantly during one or more of the observations. However, with observation durations of ∼3 h and a stellar rotation period of 10.5 d, the visible portion of the stellar surface will have changed little during any one observation. To first order, the resulting small impact on the occultation light curves can be modelled as a linear trend, which will be handled by the trend functions. Another concern is that the stellar brightness may have changed significantly between the non-simultaneous occultation observations. For example, the 3.6-μm data were obtained two months after the 4.5-μm data and it is the relative measurements at these two wavelengths that are the prime diagnostic for the presence of an atmospheric temperature inversion. Assuming a constant planet brightness, the stellar brightness would need to have changed by ∼5 per cent to have changed the occultation depth by 1σ and the amplitude of the modulation of the WASP light curves (a few mmag) shows that this is very unlikely. Thus, our derived eclipse depths, and the conclusions on which they depend, are insensitive to the variability of WASP-19.

4 DISCUSSION

4.1 Atmosphere model

We interpret our observations of the hot Jupiter WASP-19b using the exoplanetary atmospheric modelling and retrieval method developed in Madhusudhan & Seager (2009, 2010, 2011). We model a plane-parallel atmosphere of WASP-19b observed in thermal emission at secondary eclipse. The dayside spectrum of the planet is generated using line-by-line radiative transfer, with constraints of hydrostatic equilibrium and global energy balance, and includes the dominant sources of infrared (IR) opacity expected in gaseous atmospheres at high temperature. Our sources of opacity include molecular absorption due to H_2O, CO, CH_4, CO_2, NH_3, TiO and VO (Rothman et al. 2005; Freedman, Marley & Lodders 2008; Karkoschka & Tomasko 2010) and H_2–H_2 collision-induced absorption (Borysow, Jorgensen & Zheng 1997; Borysow 2002). The concentrations of the species and the pressure–temperature (P–T) profile constitute the free parameters in the model (Madhusudhan & Seager 2009). We explore the parameter space of the model using an MCMC scheme (see Madhusudhan & Seager 2010, 2011), and constrain regions of parameter space consistent with the measured planet-to-star flux density ratios at different levels of fit. Our goal is to constrain the existence of a possible temperature inversion, the dayside-to-nightside redistribution efficiency, the concentrations of the different molecular species and the C/O ratio (e.g. Madhusudhan et al. 2011a) in the dayside atmosphere of WASP-19b. In what follows, we discuss model solutions that explain the data within the 1σ observational uncertainties, as shown in Fig. 4.

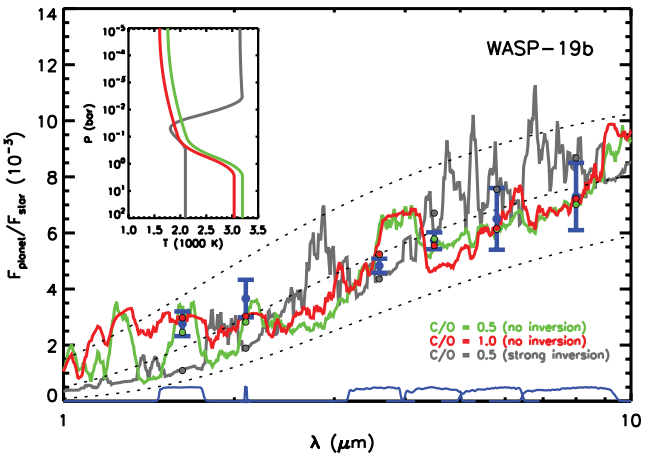

Figure 4. Observations and model spectra of thermal emission from WASP-19b. The blue circles with error bars show our observed planet-to-star flux density ratios reported in this work. The transmission curves for the corresponding photometric bandpasses are shown by the blue curves along the abscissa. The red, green and grey curves in the main panel show model spectra of WASP-19b, and the same-coloured curves in the inset show the temperature profiles of the corresponding models. The red, green and grey circles in the main panel show the corresponding model spectra integrated in the observed bandpasses for comparison with data. The data indicate the absence of a strong temperature inversion. The green and red curves show two models without thermal inversions but with different chemical composition, C/O ratios of 0.5 (O-rich) and 1.0 (C-rich), respectively, both of which fit the data well. On the other hand, the grey model, which has a strong thermal inversion, provides a poor fit to the data, especially at 1.6, 2.09 and 4.5 μm. The three dotted lines show model blackbody spectra of WASP-19b with temperatures of 1800, 2500 and 2900 K, shown for reference.

4.2 Temperature inversion

The data indicate the lack of a strong temperature inversion in the dayside atmospheres of WASP-19b. The observations and two models fitting the data are shown in Fig. 4. The lack of a temperature inversion in WASP-19b is evident from the data even without detailed modelling. First, the brightness temperature in the 4.5-μm channel, $T_{\rm b,\,4.5}$, is lower than that in the 3.6 μm channel, $T_{\rm b,\,3.6}$ (Table 3). The presence of a temperature inversion is often indicated by a $T_{\rm b,\,4.5}$ value considerably higher than the $T_{\rm b,\,3.6}$ value, due to strong CO emission and some H_2O emission in the 4.5-μm channel (Burrows, Budaj & Hubeny 2008; Fortney et al. 2008; Madhusudhan & Seager 2010). Secondly, the brightness temperatures at 1.6 and 2.09 μm are larger than those in all four IRAC channels, which are at longer wavelengths. Since the bands at 1.6 and 2.09 μm are windows in molecular opacity, they are expected to probe temperatures in deeper layers of the atmosphere compared to any of the IRAC channels. Therefore, the high temperatures in the 1.6- and 2.09-μm bands compared to all the IRAC channels imply temperature decreasing outwards in the atmosphere, and hence the absence of a temperature inversion or, at most, the presence of one too weak to be detectable with the available data. Two model *P*–*T* profiles without temperature inversions and the corresponding model spectra are shown in Fig. 4. All the IRAC data can be explained by molecular absorption in the atmosphere due to the temperature decreasing outwards. Also shown in Fig. 4 is a model with a strong thermal inversion (grey model) which predicts significantly lower fluxes at 1.6 and 2.09 μm and higher fluxes at 4.5 μm than those observed. Consequently, such strong inversions are ruled out by the data.

The lack of a strong temperature inversion in WASP-19b offers a new constraint on existing classification schemes of irradiated giant exoplanets. WASP-19b falls in the category of highly irradiated hot Jupiters which have been predicted to host temperature inversions due to TiO and VO, assuming solar abundances (Fortney et al. 2008) – the so called TiO/VO hypothesis. However, our finding of a lack of a strong temperature inversion in WASP-19b implies that either TiO and VO are depleted or an entirely different process is at play. If the composition is oxygen rich, the lack of a strong temperature inversion in WASP-19b can be explained if TiO and VO are depleted in the upper atmosphere due to gravitational settling, which can be significant if the vertical mixing is weak (Spiegel et al. 2009). On the other hand, if the composition is carbon rich, TiO and VO would be naturally scarce (Madhusudhan et al. 2011b).

Knutson et al. (2010) posit that the high UV flux impinging on those planets orbiting chromospherically active stars could destroy the high-opacity, high-altitude compounds that would otherwise lead to temperature inversions. With $\log R'_{\rm HK} = -4.50 \pm 0.03$, WASP-19 has a similar activity level to that of the handful of other stars around which hot Jupiters without temperature inversions ($\log R'_{\rm HK} = -4.9$ to -4.5) are known to orbit. Those planets thought to have inversions orbit quieter stars, with $\log R'_{\rm HK} = -5.4$ to -4.9. Thus, our finding that WASP-19b lacks a strong inversion supports the hypothesis of Knutson et al. (2010) and usefully adds to the handful of such systems known. *Spitzer* routinely measures the thermal emission of planets at 3.6 and 4.5 μm. For planets with temperature inversions, CO and water switch from absorption to emission, resulting in a higher flux in the 4.5-μm band, in which these molecules have features. Knutson et al. (2010) proposed a model-independent, empirical metric for classifying hot Jupiters, which we denote with ζ. This is the gradient of the measurements at 3.6 and 4.5 μm, i.e. $(\Delta F_{4.5} - \Delta F_{4.5})/0.9$ μm, minus the gradient of the blackbody that is the best fit to the two measurements. A positive ζ-value would suggest an inverted atmosphere and a strongly negative ζ-value would indicate a non-inverted atmosphere; Knutson et al. (2010) suggest a delineation around $\zeta = -0.05$ per cent μm^{-1}. For WASP-19b, we calculated $\zeta = -0.031 \pm 0.043$ per cent μm^{-1}. This value is at the border between inversion and no-inversion and therefore is consistent with our finding that WASP-19b does not have a strong inversion.

We note that in their activity-inversion plot (their fig. 5), Knutson et al. (2010) omit XO-3 but include TrES-4, HAT-P-7 and WASP-18, all of which have $T_{\rm eff} \gtrsim 6200$. XO-3b has a temperature inversion and XO-3 has a $\log R'_{\rm HK}$ index indicative of activity, which seems to contradict the activity-inversion hypothesis. The other three planets have inversions and orbit quiet stars. Knutson et al. (2010) concluded that in fact XO-3 is likely to be chromospherically quiet, based on a visual inspection of their spectrum and having noted that the $\log R'_{\rm HK}$ calibration is unreliable for stars with $T_{\rm eff} \gtrsim 6200$. Perhaps then TrES-4, HAT-P-7 and WASP-18 are also suspect since they also have $T_{\rm eff} \gtrsim 6200$.

4.3 Atmospheric composition

We find that the observations can be explained by models with oxygen-rich as well as carbon-rich compositions. The absorption in the near-IR (1.6- and 2.09-μm) bands is minimal due to the lack of major molecular features. The constraints on the composition come primarily from the IRAC data, which together encompass features of CO, H_2O, CH_4 and CO_2. The near-IR data, however, are critical to constraining the temperature of the lower atmosphere and thus are key in anchoring the model-atmosphere spectra to the measured SED. Two models with different C/O ratios, C/O = 0.5 (oxygen rich) and C/O = 1 (carbon rich), are shown in Fig. 4. As demonstrated in Madhusudhan et al. (2011b), CO is a dominant carbon-bearing molecule in both C-rich and O-rich regimes. Consequently, the 4.5-μm absorption in both models in Fig. 4 is caused primarily by CO absorption; in the O-rich model CO_2 contributes additional absorption in this channel. The absorption in the 3.6-, 5.8- and 8.0-μm IRAC channels in the O-rich model is caused primarily by H_2O absorption, whereas absorption in the C-rich model is caused by a combination of H_2O and CH_4 absorption; H_2O is depleted by a factor of 100 and CH_4 is enhanced by a factor of 1000 with respect to the O-rich model, both of which are chemically feasible (Madhusudhan et al. 2011b). The principal difficulty in differentiating between the two models with the current data are the large uncertainties in the 5.8- and 8.0-μm IRAC data. For example, a high 5.8-μm point would indicate low water absorption, and hence high C/O, as demonstrated in Madhusudhan et al. (2011a). New observations in the near-IR can differentiate between spectra from the carbon-rich and oxygen-rich compositions (e.g. Madhusudhan et al. 2011a). The water abundance can be measured via transmission spectroscopy of the 1.4-μm water band using the G141 grism of HST/WFC3; these observations were recently performed for WASP-19b by Deming (2009). We could measure, or at least place useful constraints on, the TiO abundance with ground-based occultation observations in the *z* and *J* bands.

4.4 Orbital eccentricity

For a circular orbit, mid-occultation occurs half an orbital period after mid-transit. We find the occultation to occur only 4^{+35}_{-30} s later than this and constrain both $e\cos\omega$ and $e\sin\omega$ to a small region around zero. Hence, the orbit is very nearly circular, though the available data do permit a small, non-zero eccentricity provided

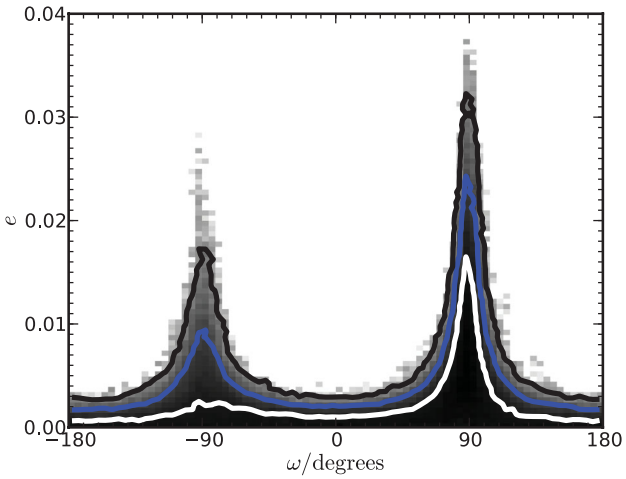

Figure 5. The MCMC posterior distributions of e and ω. The white, blue and black contours are, respectively, the 1, 2 and 3σ confidence limits. The shading of each bin is proportional to the logarithm of the number of MCMC steps within. The available data exclude large values of e for any orbital orientation, and only very small values of e are permitted unless $|\omega| \approx 90$.

that the major axis of the orbit is near-aligned with our line of sight, such that the occultation time is not affected (i.e. $|\omega| \approx 90$; Fig. 5). We place a 3σ upper limit on eccentricity of $e < 0.027$.

Hot Jupiters are considered to have been moved inwards to close orbits through planet–planet scattering or by the Kozai mechanism and tidal circularization (e.g. Batygin, Morbidelli & Tsiganis 2011; Naoz et al. 2011; Wu & Lithwick 2011). However, for the very shortest period systems, such as WASP-19b, it is unlikely that they could have been moved directly to their current orbit, since that would have required careful fine-tuning to avoid destruction by collision with the star. Thus, most likely WASP-19b was first moved to an orbit near ∼2 Roche radii and has since spiralled inwards through tidal orbital decay (see Guillochon, Ramirez-Ruiz & Lin 2011 and the discussion of WASP-19b specifically in Hellier et al. 2011).

From tidal theory, the circularization of a hot Jupiter's orbit is thought to proceed much faster than the infall, and this is consistent with the observation that hot Jupiters tend to be in circular orbits. Thus, the suggestion that WASP-19b has undergone significant tidal decay, from ∼2 Roche radii to the current 1.2 Roche radii, leads to the expectation that the current eccentricity will be essentially zero, in line with our results.

ACKNOWLEDGEMENTS

This work is based on observations made with the *Spitzer Space Telescope*, which is operated by the Jet Propulsion Laboratory, California Institute of Technology under a contract with NASA. We thank N. P. Gibson for providing the HAWK-I 2.09-μm light curve.

REFERENCES

Anderson D. R. et al., 2010, A&A, 513, L3
Anderson D. R. et al., 2011a, A&A, 534, A16
Anderson D. R. et al., 2011b, MNRAS, 416, 2108
Anderson D. R. et al., 2012, MNRAS, 422, 1988
Barman T. S., Hauschildt P. H., Allard F., 2005, ApJ, 632, 1132
Batygin K., Morbidelli A., Tsiganis K., 2011, A&A, 533, A7
Boisse I. et al., 2009, A&A, 495, 959
Borysow A., 2002, A&A, 390, 779
Borysow A., Jorgensen U. G., Zheng C., 1997, A&A, 324, 185
Burrows A., Budaj J., Hubeny I., 2008, ApJ, 678, 1436
Campo C. J. et al., 2011, ApJ, 727, 125
Charbonneau D. et al., 2005, ApJ, 626, 523
Charbonneau D., Knutson H. A., Barman T., Allen L. E., Mayor M., Megeath S. T., Queloz D., Udry S., 2008, ApJ, 686, 1341
Collier Cameron A. et al., 2007, MNRAS, 380, 1230
Cowan N. B., Agol E., 2011, ApJ, 729, 54
Croll B., Lafreniere D., Albert L., Jayawardhana R., Fortney J. J., Murray N., 2011, AJ, 141, 30
de Mooij E. J. W., Snellen I. A. G., 2009, A&A, 493, L35
Deming D., 2009, in HST Proposal 12181
Deming D., Seager S., Richardson L. J., Harrington J., 2005, Nat, 434, 740
Désert J.-M., Lecavelier des Etangs A., Hébrard G., Sing D. K., Ehrenreich D., Ferlet R., Vidal-Madjar A., 2009, ApJ, 699, 478
Enoch B., Collier Cameron A., Parley N. R., Hebb L., 2010, A&A, 516, A33
Fazio G. G. et al., 2004, ApJS, 154, 10
Ford E. B., 2006, ApJ, 642, 505
Fortney J. J., Lodders K., Marley M. S., Freedman R. S., 2008, ApJ, 678, 1419
Freedman R. S., Marley M. S., Lodders K., 2008, ApJS, 174, 504
Fressin F., Knutson H. A., Charbonneau D., O'Donovan F. T., Burrows A., Deming D., Mandushev G., Spiegel D., 2010, ApJ, 711, 374
Gibson N. P. et al., 2010, MNRAS, 404, L114
Gillon M. et al., 2007, A&A, 471, L51
Guillochon J., Ramirez-Ruiz E., Lin D., 2011, ApJ, 732, 74
Hauschildt P. H., Allard F., Baron E., 1999, ApJ, 512, 377
Hebb L. et al., 2010, ApJ, 708, 224
Hellier C., Anderson D. R., Collier-Cameron A., Miller G. R. M., Queloz D., Smalley B., Southworth J., Triaud A. H. M. J., 2011, ApJ, 730, L31
Ibgui L., Burrows A., Spiegel D. S., 2010, ApJ, 713, 751
Karkoschka E., Tomasko M. G., 2010, Icarus, 205, 674
Knutson H. A., Charbonneau D., Allen L. E., Burrows A., Megeath S. T., 2008, ApJ, 673, 526
Knutson H. A., Charbonneau D., Cowan N. B., Fortney J. J., Showman A. P., Agol E., Henry G. W., 2009, ApJ, 703, 769
Knutson H. A., Howard A. W., Isaacson H., 2010, ApJ, 720, 1569
Machalek P., McCullough P. R., Burke C. J., Valenti J. A., Burrows A., Hora J. L., 2008, ApJ, 684, 1427
Madhusudhan N., Seager S., 2009, ApJ, 707, 24
Madhusudhan N., Seager S., 2010, ApJ, 725, 261
Madhusudhan N., Seager S., 2011, ApJ, 729, 41
Madhusudhan N. et al., 2011a, Nat, 469, 64
Madhusudhan N., Mousis O., Johnson T. V., Lunine J. I., 2011b, ApJ, 743, 191
Mamajek E. E., Hillenbrand L. A., 2008, ApJ, 687, 1264
Nagasawa M., Ida S., 2011, ApJ, 742, 72
Naoz S., Farr W. M., Lithwick Y., Rasio F. A., Teyssandier J., 2011, Nat, 473, 187
Noyes R. W., Weiss N. O., Vaughan A. H., 1984, ApJ, 287, 769
Pollacco D. L. et al., 2006, PASP, 118, 1407
Pollacco D. et al., 2008, MNRAS, 385, 1576
Press W., Flannery B., Teukolsky S., Vetterling W., 1992, Numerical Recipes in C: The Art of Scientific Computing. Cambridge Univ. Press, Cambridge
Rothman L. S. et al., 2005, J. Quant. Spectrosc. Radiat. Transfer, 96, 139
Santos N. C., Mayor M., Naef D., Pepe F., Queloz D., Udry S., Blecha A., 2000, A&A, 361, 265
Sing D. K., López-Morales M., 2009, A&A, 493, L31
Smith A. M. S., Anderson D. R., Skillen I., Collier Cameron A., Smalley B., 2011, MNRAS, 416, 2096
Smith A. M. S. et al., 2012, A&A, 545, A93
Spiegel D. S., Silverio K., Burrows A., 2009, ApJ, 699, 1487
Werner M. W. et al., 2004, ApJS, 154, 1
Wu Y., Lithwick Y., 2011, ApJ, 735, 109
Zahnle K., Marley M. S., Freedman R. S., Lodders K., Fortney J. J., 2009, ApJ, 701, L20

This paper has been typeset from a TEX/LATEX file prepared by the author.